Acta Pharmaceutica Sinica B 2025;15(5):2673−2686

Chinese Pharmaceutical Association
Institute of Materia Medica, Chinese Academy of Medical Sciences

Acta Pharmaceutica Sinica B

www.elsevier.com/locate/apsb
www.sciencedirect.com

ORIGINAL ARTICLE

Sulfafurazole dimers potentiate chemo-immunotherapy of low immunogenic breast cancer by preventing the PD-L1 exosomes secretion

Zheng Wang, Ronghui Yin, Lin Zhang, Shiyu Li, Zhanwei Zhou*, Minjie Sun*

NMPA Key Laboratory for Research and Evaluation of Pharmaceutical Preparations and Excipients, State Key Laboratory of Natural Medicines, Department of Pharmaceutics, China Pharmaceutical University, Nanjing 210009, China

Received 28 October 2024; received in revised form 10 January 2025; accepted 20 February 2025

KEY WORDS

Carrier free nanomedicine;
Exosomes depletion;
Immunogenic cell death;
Chemo-immunotherapy;
GSH responsive delivery system;
Programmed death ligand 1;
T cells exhaustion;
Breast cancer

Abstract The αPD-L1 antibody-based immune checkpoint blockade therapy is still limited by the poor clinical response rate as it is mainly utilized to block surface PD-L1 on tumor cells while ignoring abundant PD-L1 exosomes secreted in the environment, causing tumor immune evasion. Here, we proposed an exosome biogenesis inhibition strategy to suppress tumor exosomes secretion from the source, reducing the inhibitory effect on T cells and enhancing chemo-immunotherapy efficacy. We developed sulfafurazole homodimers (SAS) with disulfide linkages, effectively releasing the drug in response to glutathione (GSH) and inhibiting 4T1 tumor-derived exosomes secretion. Subsequently, gemcitabine (Gem) was encapsulated to induce immunogenic cell death (ICD). Consequently, Gem@SAS inhibited the secretion of tumor exosomes by more than 70%, increased proliferation and granzyme B secretion ability of T cells by more than 2 times, and showed superior efficacy in breast cancer treatment as well as lung metastasis of breast cancer.

*Corresponding authors.
E-mail addresses: zwzhou@cpu.edu.cn (Zhanwei Zhou), msun@cpu.edu.cn (Minjie Sun).

Peer review under the responsibility of Chinese Pharmaceutical Association and Institute of Materia Medica, Chinese Academy of Medical Sciences.

https://doi.org/10.1016/j.apsb.2025.03.007

1. Introduction

For a long time, tumor cells were believed to evade immune surveillance by up-regulating the expression of PD-L1 on their surfaces, which inhibited T cells functions by binding to the PD-1 receptor on T cells. Over the past decade, immune checkpoint blockade (ICB) therapy represented by PD-1/PD-L1 has been used to target tumor cells or T cells for treatment, benefiting patients a lot[1-3]. However, clinical research has shown that the overall response rate to ICB therapy remains below 30%[4]. Regarding this issue, recent research has identified that in addition to membrane bound PD-L1, exosomes secreted by tumor cells carrying PD-L1 proteins similarly inhibit T cells functions, thereby leading to immune escape. This finding partly explains the failure of ICB therapy[5-7].

Exosomes are a class of extracellular vesicles originating from endosomes, which could carry cellular contents such as proteins, mRNA, DNA, miRNA, and various molecules that can be passed between cells[8,9]. Exosomes secreted by various cells within the tumor microenvironment can significantly facilitate the occurrence and progression of cancer. For example, exosomes derived from cancer-associated fibroblasts (CAFs) inhibited oxidative phosphorylation and promoted glycolysis and glutamine-dependent reductive carboxylation, thereby altering cancer cell metabolism[10]. Tumor-associated macrophages (TAMs) derived exosomes were rich in miR-29a-3p and miR-21-5p[11]. These microRNAs modulated the ratio of Treg/Th17 cells through the suppression of STAT3, thereby promoting an immune-suppressive microenvironment that accelerated the progression and metastasis of cancer. Tumor cell derived exosomal circular RNAs, miRNAs and many other components played a vital role in modulating T cell function. Among them, tumor cell derived exosomal PD-L1 possessed both major histocompatibility complex (MHC) and PD-L1 molecules, which binded to T cell receptor and PD-1 molecules on T cells, leading to T cell dysfunction[12]. Moreover, PD-L1 exosomes could flow to distal tissues along with blood circulation, creating immunosuppressive microenvironment conducive to immune escape of tumor cells[13-15]. Additionally, PD-L1 exosomes in blood circulation can act as decoys to sequester αPD-L1, thereby diminishing efficacy of αPD-L1[16-18]. Consequently, strategies aimed at inhibiting tumor exosomes could effectively alleviate the formation of immunosuppressive microenvironment and promote tumor killing effect of T cells, which is of great significance for potentiating PD-L1/PD-1 mediated immunotherapy to inhibit the development of tumors[19,20].

Currently, three main approaches are employed to control tumor exosomes: inhibiting biogenesis of exosomes, removing exosomes from circulatory system and preventing uptake of exosomes by target cells[21]. In terms of inhibiting exosomes biogenesis, a series of small molecule drugs or siRNA drugs have been developed for different targets[22]. Among them, sulfafurazole has been proven to reduce the secretion of exosomes by inhibiting endothelin A and down-regulating intracellular Rab27a expression, and has demonstrated significant anti-tumor abilities as well as anti-metastatic abilities in mouse models of breast cancer xenografts, providing a strategy to address tumor escape from immune surveillance[23,24].

At present, a substantial number of studies have been conducted regarding the cell death pathway, and numerous mechanisms have been identified, including ferroptosis, pyroptosis, autophagy and so on[25,26]. Among them, immunogenic cell death (ICD) is a kind of regulated cell death (RCD), which is triggered by specific chemotherapy drugs, oncolytic virus, phototherapy, radiotherapy and so on[27,28]. This form of cell death has been shown to effectively stimulate an immune response against cancer in immunocompetent hosts. For example, cells undergoing immunogenic death release a range of damage associated molecular patterns (DAMPs). The released DAMPs bind to antigen presenting cells (APCs), prompting them to recognize and phagocytose tumor antigens. APCs then migrate to the lymph nodes, where they cross-present tumor antigens to T cells, thereby activating a tumor-specific immune response. In the process of ICD, the secondary killing of tumor cells by T cells is a crucial component, and addressing the obstruction of T cell function by PD-L1 exosomes is important for potentiating ICD-induced immune efficacy[29].

The emergence of diverse forms of nanomedicines, including liposomes, albumin nanoparticles, polymer nanoparticles, and biomimetic cell membrane nanoparticles, has spurred rapid progress in the field of life medicine[30,31]. Among them, carrier-free nanomedicines, where the drug itself acts as a carrier and forms nano-delivery systems through self-assembly between free drugs, prodrugs, or non-drug agents, have been widely employed in drug delivery research in recent years[32-34]. Carrier-free nanomedicines have high biosafety and can effectively circumvent the toxicity and immunogenicity problems caused by carriers. Meanwhile, carrier-free nanomedicines are simple in composition, easy to prepare, and have a high drug loading rate (close to 100%). Moreover, the nanoscale property can prolong the blood circulation time of the drug and increase the accumulation of the drug in the tumor tissue[35,36]. In conclusion, this flexible and simple nanomedicine is expected to become a universal drug platform for cancer clinical treatment in the future.

Inspired by above considerations, we exploited the property of sulfafurazole to inhibit tumor exosomes secretion to enhance chemotherapy-induced immunotherapy and thereby enable combination therapy. Sulfafurazole was modified on both sides of dithiobispropionic acid to construct a disulfide-linked sulfafurazole homodimer (SAS), which was subsequently encapsulated with the chemotherapeutic agent gemcitabine to form Gem@SAS co-assembled nanoparticles (Scheme 1A). In tumor tissues, high levels of glutathione cause disulfide bond cleavage to release drugs. Low-dose gemcitabine acts as an ICD initiator to induce tumor immunogenic cell death, and sulfafurazole inhibits PD-L1 exosomes release by down-regulating intracellular Rab27a levels. In lymph nodes, due to a decrease in the amount of PD-L1 exosomes, the killing ability and vitality of $CD8^+$ T cells are enhanced, and the immune efficacy induced by gemcitabine is also improved (Scheme 1B). Gem@SAS effectively inhibits the secretion of exosomes from tumor cells while enhancing the immunogenicity of tumor cells, providing an effective strategy for anti-tumor immunotherapy.

2. Materials and methods

2.1. Materials

Sulfafurazole (B24367, SFX) and 3,3′-dithiobispropionic acid (S70112) were purchased from Yuanye Bio-Technology (Shanghai, China). Gemcitabine (E080312, Gem), chlorin e6 (E082405, Ce6) and glutathione (E120083, GSH) were purchased from Energy Chemical (Shanghai, China). Annexin V-FITC/PI cell apoptosis assay kits (40302 ES), CFDA SE cell proliferation and cell tracking kit (40714 ES) and RBC lysis buffer (40401 ES)

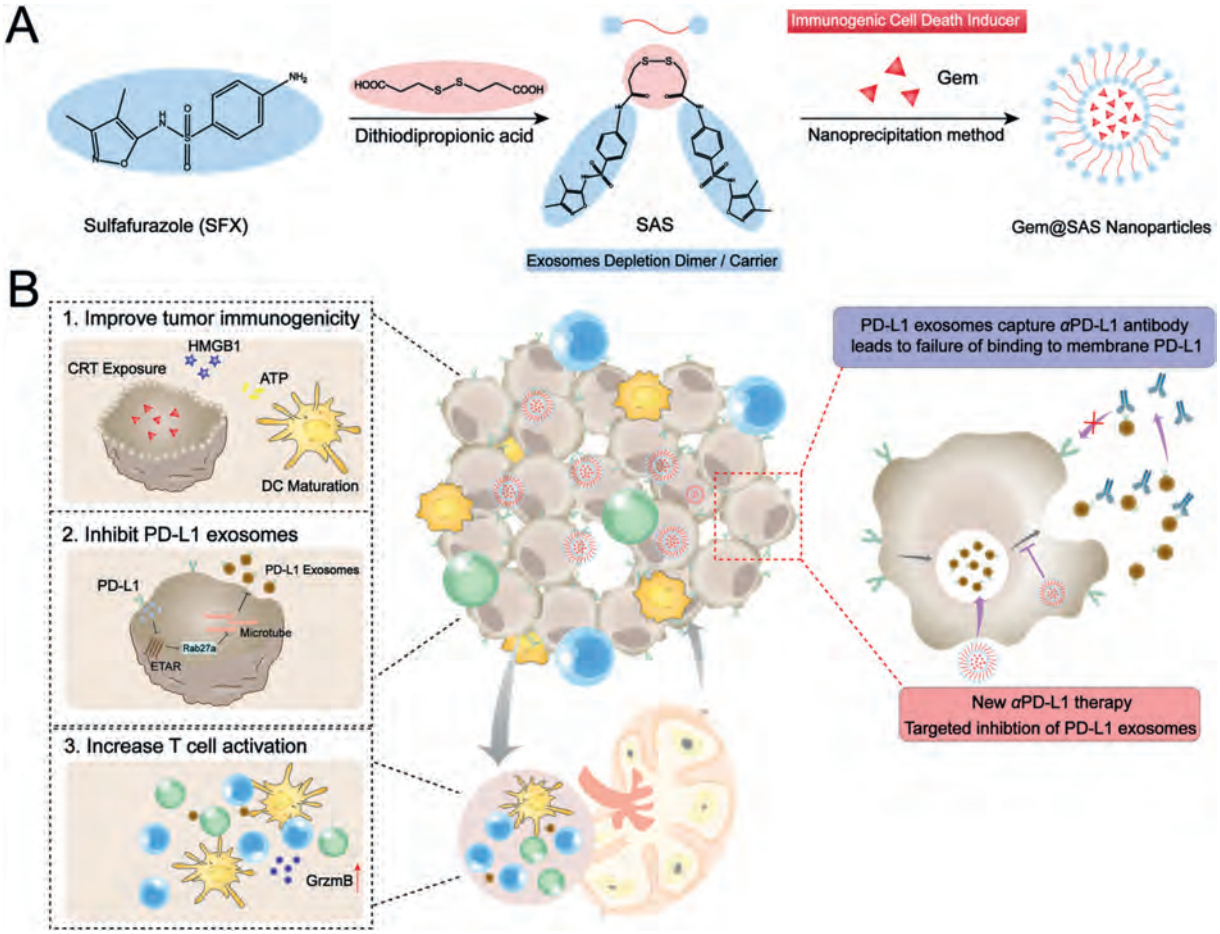

Scheme 1 Illustration of Gem@SAS for enhancing antitumor immunity by reshaping tumor immune microenvironment. (A) The synthesis of SAS and the preparation of Gem@SAS nanoparticles. (B) Gem@SAS could respond to high concentration of GSH in tumor to release gemcitabine and sulfafurazole, thereby improving tumor immunogenicity, inhibiting exosomes release and further increase T cell activation.

were purchased from Yeasen (Shanghai, China). BCA protein assay kit (P0010) and ATP assay kit (S0027) were purchased from Beyotime Biotechnology (Shanghai, China). PBS (KGL2206), DMEM (KGL1206) and RMPI-1640 medium (KGL1501) were purchased from KeyGEN BioTECH (Nanjing, China). HMGB1 ELISA kit (XY9M0382) was purchased from X−Y Biotechnology (Shanghai, China). Anti-calreticulin antibody (77344) was purchased from Cell Signaling Technology (Boston, MA, USA). MojoSort mouse CD3 T cell isolation kit (480024), purified anti-mouse CD3 antibody (100201), purified anti-mouse CD28 antibody (102101), anti-mouse MHC-Brilliant Violet 421™ (109913), anti-CD11c-PE (117307), anti-CD80-FITC (104705), anti-CD86-APC (159215), Brilliant Violet 421™ anti-mouse CD45 (147719), PE anti-mouse CD3 (100205), APC anti-mouse CD8α (162303), FITC anti-mouse CD4 (100405) and PE/Cyanine7 anti-mouse Granzyme B antibody (396410) were purchased from Biolegend (San Diego, CA, USA). Anti-PD-L1 (2B11D11) and anti-GAPDH antibodies (1E6D9) were purchased from Proteintech (Chicago, IL, USA). Cytofix/Cytoperm buffer was purchased from BD Biosciences (Andover, MA, USA). Anti-CD63 antibody (BS1523R) was purchased from Bioss (Beijing, China). ECL solution (E41104) was purchased from Vazyme Biotech Co., Ltd. (Nanjing, China). All primers were purchased from GenScript (Nanjing, China). TNF-α (EK282HS) and IFN-γ ELISA kit (EK280HS) were purchased from Liankebio (Hangzhou, China). GlutaMax (35050061) was purchased from Gibco (Shanghai, China). Mouse IL-2 recombinant protein (CK24) was purchased from Novoprotein (Suzhou, China).

2.2. *Cell lines and mice*

The mouse breast cancer cell line 4T1 and mouse dendritic cell line DC2.4 were from PerkinElmer (Waltham, MA, USA) and cultured in RMPI-1640 containing 10% FBS at 37 °C incubators with 5% CO_2. BALB/c mice (4−8 weeks, female) were provided by the Experimental Animal Centre of Yangzhou University (Yangzhou, China). All animal experiments followed the regulations of the Institutional Animal Care and Use Committee of China Pharmaceutical University (Approval No. SYXK2021-0011) and the Science and Technology Department of Jiangsu Province approved protocols.

2.3. *Synthesis and characterization of SAS*

First, dithiodipropionyl chloride was prepared as described. Briefly, dithiodipropionic acid (500 mg) was weighed in a 100 mL round-bottomed flask, with adding of 20 mL anhydrous dichloromethane and 2 mL thionyl chloride, and then added 2 drops of anhydrous *N*, *N*-dimethylformamide to catalyze the reaction. The reaction was carried out at 40 °C in a water bath with

heating and stirring under reflux conditions until the reaction solution was clarified. Then, the reaction solution was evaporated under reduced pressure to remove the solvent to obtain a light-yellow liquid product. After that, sulfafurazole (1.27 g) was weighed in another 100 mL round-bottomed flask, with adding of 10 mL anhydrous dichloromethane and anhydrous triethylamine (660 μL), then dithiodipropionyl chloride was added drop by drop under ice bath. The progress was monitored by thin-layer chromatography (TLC), and the reaction mixture were purified by silica gel column. After vacuum drying, the chemical structure of SAS was validated by nuclear magnetic resonance spectrograph (Avance AV-500, Bruker, Billerica, MA, USA) and mass spectrograph (1260−6230 TOF LC−MS, Aglient, Santa Clara, CA, USA).

2.4. Preparation and characterization of SAS and Gem@SAS NPs

The SAS NPs were prepared by nanoprecipitation method. Briefly, for SAS NPs, 20 μL SAS (dissolved in DMSO, 25 mg/mL) was added dropwise into 1 mL deionized water with stirring. To prepare gemcitabine loaded SAS NPs, gemcitabine (5 mg/mL, 5 μL) was dissolved in DMSO solution, mixed and incubated with 20 μL SAS for 30 min. Afterward, the mixture solution was added into 1 mL of deionized water with stirring. The unencapsulated drugs were removed by ultrafiltration (SL-16R, ThermoFisher, Waltham, MA, USA) with 5000 rpm for 15 min.

The serum stability of SAS NPs was investigated in RMPI-1640 medium containing 10% FBS. Particle size and zeta potential of SAS NPs were measured by Zetasizer Nano ZSE (Malvern, Marlow, UK), and the morphology of SAS NPs was observed by transmission electron microscopy (TEM, H-600, Hitachi, Tokyo, Japan).

The encapsulation efficiency and drug loading of Gem was quantified by UV spectrum (UV 1800 PC, Mapada, Shanghai, China). The content of unencapsulated Gem in the filtrate after ultrafiltration was detected and the detection of UV signal was achieved at 268 nm. The drug loading and encapsulation efficiency were calculated as shown in Eqs. (1) and (2):

$$\text{Drug loading}\ (\%) = \frac{(\textit{Total amount of Gem added} - \textit{Free Gem})}{\textit{Weight of Gem@SAS}} \times 100 \quad (1)$$

$$\text{Encapsulation efficiency}\ (\%) = \frac{(\text{Total amount of Gem added} - \text{Free Gem})}{\text{Total amount of Gem added}} \times 100 \quad (2)$$

2.5. Cellular uptake of SAS NPs

4T1 cells (1×10^4) were seeded on confocal dishes overnight. The medium was replaced with blank medium including free Ce6, Ce6@SAS NPs containing equivalent concentration of Ce6 (1 μg/mL). After incubation for 4 h, the cells were washed and fixed with paraformaldehyde. Then, the cells were stained by Hoechst 33342. The prepared confocal dishes were observed by CLSM (LSM700, Zeiss, Oberkochen, Germany). For quantitative analysis, the cells were washed, collected, and resuspended in PBS after incubation with Ce6 or Ce6@SAS NPs. Cellular uptake was analyzed by flow cytometry (Cytoflex S, Beckman, Pasadena, CA, USA).

2.6. In vivo distribution of SAS NPs

The 4T1 bearing mice were randomly divided into 3 groups ($n = 3$). When the tumor size reached 200 mm^3, free Ce6 and Ce6@SAS NPs were administered by i.v. injection at a dose equivalent to Ce6 (1 mg/kg). The mice were observed by *in vivo* image system (IVIS Spectrum, PerkinElmer, Waltham, MA, USA) 24 h post-injection. The ex-organs were also harvested and imaged at 24 h post-injection of free Ce6 and Ce6@SAS NPs.

2.7. Isolation and stimulation of $CD3^+$ T cells

Spleens were harvested from BALB/c mice (4−8 weeks, female), mechanically dissociated and passed through a 70 μm cell strainer to obtain single-cell suspensions. Red blood cells were removed using RBC lysis buffer. Then $CD3^+$ T cells were enriched using a mouse naïve $CD3^+$ T cells isolation kit, according to the manufacturer's instruction. Isolated $CD3^+$ T cells were activated for 24 h with CD3 and CD28 antibody. Subsequent T cell culture medium added GlutaMAX (1%), IL-2 (200 U/mL) and 2-Hydroxy-1-ethanethiol (55 mmol/L).

2.8. In vitro T cell assays

For CFSE proliferation assay, $CD3^+$ T cells extracted above were stained with Carboxyfluorescein diacetate, succinimidyl ester (CFDA-SE) according to CFDA SE Cell Proliferation and Cell Tracking Kit. After staining, $CD3^+$ T cells were activated with CD3/CD28 antibody. Then $CD3^+$ T cells were incubated with tumor exosomes after different pre-treatments for 48 h. T cells were collected and analyzed by flow cytometry (Beckman).

For intracellular granzyme B detection, $CD3^+$ T cells were activated with CD3/CD28 antibody first. Then $CD3^+$ T cells were incubated with tumor exosomes after different pre-treatments for 48 h. T cells were collected and treated with monensin for additional 6 h, and stained with APC anti-mouse CD8α and FITC anti-mouse CD4. Then surface stained T cells were fixed and permeabilized with Cytofix/Cytoperm buffer, and stained with PE/Cy7 anti-mouse Granzyme B antibodies. T cells were collected and analyzed by flow cytometry (Beckman).

2.9. Western blotting analysis

The main protein expressions of exosomes were investigated by Western blot. Briefly, 4T1 cells were seeded into T75 cell culture flask. Enriched exosomes were isolated by ultracentrifugation (Optima XE-100, Beckman, Pasadena, CA, USA) with 100,000×g for 2 h from 4T1 cells supernatant after diverse treatments. Subsequently, exosomes were lysed by RIPA lysis buffer and centrifuged to collect the proteins. The protein samples were then run on a 10% SDS-PAGE gel to separate the different molecular weight proteins, and then transferred to the PVDF membrane. The

membranes were blocked by 5% non-fat dry milk and incubated with the primary antibodies overnight, including CD63, PD-L1 and GAPDH. HRP conjugated secondary antibody was then incubated with the membrane for 45 min after washing 3 times with TBST buffer (10 min per time). The bands were observed by ECL chemiluminescence (Tanon 5200, Tanon, Shanghai, China).

2.10. *In vitro Rab27a silencing*

4T1 cells were seeded on 6-well plates (1×10^5 cells/well) and cultured for 24 h. Then 4T1 cells were incubated with SAS NPs for 24 h. The Rab27a mRNA level was determined by real-time PCR with β-actin as the internal control.

2.11. *GSH responsive drug release*

For release study, 1 mL Gem@SAS or SAS (1 mg/mL) was placed into a dialysis bag (MWCO: 10,000−14,000 Da) and dialysis against release medium, including pH7.4 PBS + 20 μmol/L GSH, pH7.4 PBS + 10 mmol/L GSH. At intervals of 0, 1, 2, 4, 6, 8, 12, 24 and 48 h, the release sample was taken from each vial and replaced with the same volume of pre-warmed fresh medium. The content of Gem and sulfafurazole in the release medium was measured by HPLC (Waters, Milford, MA, USA).

2.12. *In vitro cytotoxicity study*

The viability of 4T1 cells was assessed by an MTT assay. Briefly, cells were cultured in 96-well plates (5×10^3/well) overnight. Then a series concentration of free Gem, SAS NPs and Gem@SAS were added into well for 24 h incubation. Then cells were washed with PBS twice and incubated with MTT (5 mg/mL in PBS) for 4 h. The generated formazan was dissolved by DMSO and detected by a microplate reader (Synergy H1, BioTek, Beijing, China) at absorbance of 490 nm.

2.13. *In vitro apoptosis study*

The apoptosis detection of 4T1 cells was assessed by Annexin V-FITC/PI double staining assay. Briefly, cells were cultured in 12 well plates (1×10^5/well) overnight. Subsequently, they were separately treated with free Gem (0.5 μg/mL), SAS (20 μg/mL), or Gem@SAS for 24 h incubation, followed by washing twice with PBS. The cells were collected for Annexin V-FITC/PI staining for 15 min before flow cytometry analysis (Beckman).

2.14. *In vitro immunogenic cell death and DC maturation detection*

The Gem associated ICD effect was investigated by surface expression of calreticulin (CRT) and extracellular release of HMGB1, ATP. Surface expression of CRT was detected by flow cytometry (Beckman). Briefly, cells were cultured in 24 well plates (5×10^4/well) overnight. Then they were separately treated with free Gem (0.5 μg/mL), SAS (20 μg/mL), or Gem@SAS for 24 h incubation. Afterward, cells were harvested and stained with CRT-APC antibody under 4 °C for 1 h, followed by flow cytometry analysis (Beckman). For quantification of released ATP and HMGB1 in medium, the medium was collected after treatment. Then the detection was performed with an ATP assay kit and an HMGB1 ELISA assay according to the manufacturer's instructions.

The induction of DC maturation was evaluated on dendritic cells (DC 2.4). Briefly, 4T1 cells (1×10^5/well) were seeded into 12 well plates and given different treatments as mentioned above. After 24 h post-treatment, the DC 2.4 cells were co-cultured with the residual 4T1 cells for an additional 24 h. After being stained with anti-CD80-FITC and anti-CD86-APC antibodies, the maturation of DC cells was examined by flow cytometry (Beckman).

2.15. *In vivo anti-tumor study*

For unilateral 4T1 xenograft model, therapies were conducted when the tumor volume reached approximately 100 mm^3. Then, mice were divided into 4 groups ($n = 5$) randomly: Saline, Gem (0.5 mg/kg), SAS (20 mg/kg) or Gem@SAS. On Days 0, 2 and 4, mice were injected intravenously with different treatment. The tumor size and body weight were measured every 2 days until Day 16. The tumor volume (V) was calculated as shown in Eq. (3):

$$V = 1/2 \times \text{Length} \times \text{Width}^2 \quad (3)$$

For survival monitoring, mice were divided into 4 groups ($n = 8$) randomly and the treatment was the same as mentioned above. The survival was monitored until Day 100.

2.16. *In vivo immune activation analysis*

For *in vivo* immune activation analysis, mice were divided into 4 groups ($n = 3$) randomly and the treatment was the same as mentioned above. On Day 7, mice were sacrificed for immune analysis. The tumor tissues were sheared into small fragments and digested with collagenase for 30 min under 37 °C. The tumor infiltrated lymphocyte cells underwent enrichment by percoll buffer and stained with Brilliant Violet 421™ anti-mouse CD45, PE anti-mouse CD3, APC anti-mouse CD8a antibodies for 1 h under 4 °C before flow cytometry analysis (Beckman). The ratio of matured DCs in the lymph nodes was also analyzed by flow cytometry (Beckman) after staining with Brilliant Violet 421™ anti-mouse MHC, anti-CD11c-PE, anti-CD80-FITC, and anti-CD86-APC antibodies. The activation of T cells was further explored by analyzing the cellular activation marker Granzyme B, and the ratio of activated T cells in lymph nodes was analyzed by flow cytometry (Beckman) after staining with Brilliant Violet 421™ anti-mouse CD45, PE anti-mouse CD3, APC anti-mouse CD8a antibodies, FITC anti-mouse CD4 antibodies and PE/Cy7 anti-mouse Granzyme B antibodies.

2.17. *In vivo anti-metastasis study*

For anti-metastasis study, 4T1 cells were injected intravenously at a concentration of 5×10^5 per mouse. Then mice were divided into 4 groups ($n = 3$) randomly and the treatment was the same as mentioned above. On Day 14, mice were sacrificed and lung tissues were harvested and fixed in Bouin's solution for 4 h, followed by taking images of the lungs. H&E assay was performed by Wuhan Servicebio Technology.

2.18. *TNF-α and IFN-γ detection*

For *in vitro* TNF-α and IFN-γ detection, 4T1 cells (1×10^5/well) were seeded into 12 well plates and given different treatments as mentioned above. After 24 h post-treatment, the DC 2.4 cells were

co-cultured with the residual 4T1 cells for an additional 24 h. The cell supernatant was collected by centrifugation and detected according to the instruction.

For *in vivo* TNF-α and IFN-γ detection, the blood of mice was collected on the third day after different treatments. Then the blood was agglutinated at 37 °C for 30 min and centrifuged to harvest serum. The cytokines in the serum were detected according to the instruction.

2.19. Statistical analysis

All statistical analyses were performed using GraphPad Prism version 9 software (San Diego, CA, USA). The results were expressed as mean ± standard deviation (SD). Student's *t*-test was used to compare two groups, and ordinary one-way ANOVA was used to compare three or more groups. *P*-value <0.05 was considered statistically significant between the data sets, where all significant values were indicated as follows: $^{*}P < 0.05$, $^{**}P < 0.01$, $^{***}P < 0.001$.

3. Results and discussion

3.1. Preparation and characterization of sulfafurazole homodimer (SAS)

The sulfafurazole homodimer was synthesized by conjugating two sulfafurazole molecules together using 3,3′-dithiobispropionic acid as the linker, and the reaction was completed within 24 h by thin-layer chromatography (TLC). ^{1}H NMR spectroscopy and mass spectroscopy were used to validate the chemical structure of SAS (Supporting Information Fig. S1). Then, the SAS nanoparticles were prepared by one-step nanoprecipitation method, and solutions displayed light blue opalescence (Fig. 1A). In addition, the SAS nanoparticles was uniform spherical structure with the particle size of nearly 160 nm detected by transmission electron microscopy (TEM) and dynamic laser scattering (DLS) (Fig. 1A and B), and the zeta potential of SAS nanoparticles increased from −23.3 to −10.9 mV compared to SAS monomers (Fig. 1C). Moreover, SAS nanoparticles could remain stable in serum, proved by particle size changed slightly within 24 h (Supporting Information Fig. S2). Due to the presence of disulfide bonds in SAS nanoparticles, which had the ability of glutathione responsive disassembly, the changes of SAS nanoparticles in solution containing glutathione were monitored by DLS and TEM (Fig. 1D and E). The particle size of SAS nanoparticles changed quickly under the reduction environment, which increased from 160 nm to nearly 500 nm (Fig. 1F). The TEM images showed the disassembly morphology of SAS nanoparticles, which was disordered and the spherical shape was destroyed. Then, we investigated the capacity of high concentration GSH to initiate drug release (Supporting Information Fig. S3). Merely a small fraction of SFX (21.44%) was released from SAS nanoparticles following incubation with 20 μmol/L GSH, which implied that the nanoparticles possessed favorable stability. When incubated with 10 mmol/L GSH, a substantial portion of SFX (65.95%) was released from SAS nanoparticles, signifying that a high concentration of GSH was capable of remarkably facilitating drug release.

We further examined the cellular uptake of SAS nanoparticles, the photosensitizer Ce6 was used as a model drug and co-assembled with SAS to form Ce6@SAS nanoparticles to evaluate the cellular uptake ability. It was found that the red fluorescence signal of Ce6@SAS was stronger than free Ce6 (Fig. 1G), which indicated that SAS nanoparticles could promote drug cellular uptake. Flow cytometry also showed similar results (Supporting Information Fig. S4), and after treating 4T1 cells with chlorpromazine as an endocytosis inhibitor, the mean fluorescence intensity (MFI) of the cells decreased by approximately 35%, suggesting that SAS may promote cellular uptake *via* the clathrin protein-mediated endocytosis pathway. What's more, we also investigated the tissue distribution and tumor accumulation of SAS nanoparticles. As visualized in Fig. 1H, the fluorescence signal of Ce6@SAS was significantly higher than that of free Ce6, which could be attributed to the passive targeting mediated by "EPR" effect. In addition, ex-organ imaging was taken 24 h after drug administration. As shown in Supporting Information Fig. S5, the fluorescence signal of Ce6@SAS was mainly distributed in the liver and tumor, with a weak distribution in other organs, further demonstrating that Ce6@SAS has tumor targeting effect. Meanwhile, the fluorescence signal of Ce6@SAS at tumor site was about three times higher than that of free Ce6, proving that the formation of nanoparticles could help to promote the accumulation of drugs in the tumor site.

3.2. SAS nanoparticles inhibited exosomes secretion in 4T1 cells

It was reported that sulfafurazole could inhibit biogenesis of exosomes by antagonizing endothelin receptor A, down-regulating intracellular Rab27a expression and other pathways (Fig. 2A). Disulfide bonds in SAS were broken in response to high concentration of GSH within the tumor, releasing sulfafurazole and enabling the inhibition of tumor-derived exosomes. The concentration of exosomes in cell culture supernatants was determined by the BCA method, and exosomes in the supernatant were dramatically decreased to 29.3% (Fig. 2B). Furthermore, the expression level of Rab27a was examined by real time PCR. The primer sequences of target gene Rab27a and the internal reference gene β-actin were shown in the Supporting Information Table S1. As shown in Fig. 2C, the expression level of Rab27a in 4T1 cells was only 18.6% of that in the control group. These results suggested that SAS could down-regulate intracellular Rab27a expression, thereby inhibiting exosomes secretion. In addition, nanoparticle tracking analysis (NTA) results showed that the particle size of exosomes extracted from tumor supernatant after PBS treatment and SAS treatment was about 120 nm, and the number of exosome particles in SAS treatment group decreased by about 50% (Fig. 2D), further demonstrating that SAS nanoparticles have the ability to inhibit the release of exosomes from 4T1 cells. Furthermore, the morphology of exosomes in cell supernatants after different treatments was observed by TEM (Fig. 2E). The results showed that SAS treatment did not affect the morphology of exosomes, and the number of exosomes in the visual field was reduced.

Studies have shown that exosomes secreted by tumor cells have the ability to inhibit the proliferation and activation of T cells, leading to immunosuppression. Therefore, in this section, the effect of 4T1 derived exosomes on T cell function was determined. Briefly, supernatant of tumor cells after different treatments were collected for co-incubation with T cells, then proliferation and expression of granzyme B were detected. In Fig. 2F and G, after stimulation with CD3/CD28 antibody, the proliferation ability of T cells was significantly improved, and the positive rate increased from 5.78% to 97.6%. However, after co-incubation of T cells with exosomes, the positive rate was only

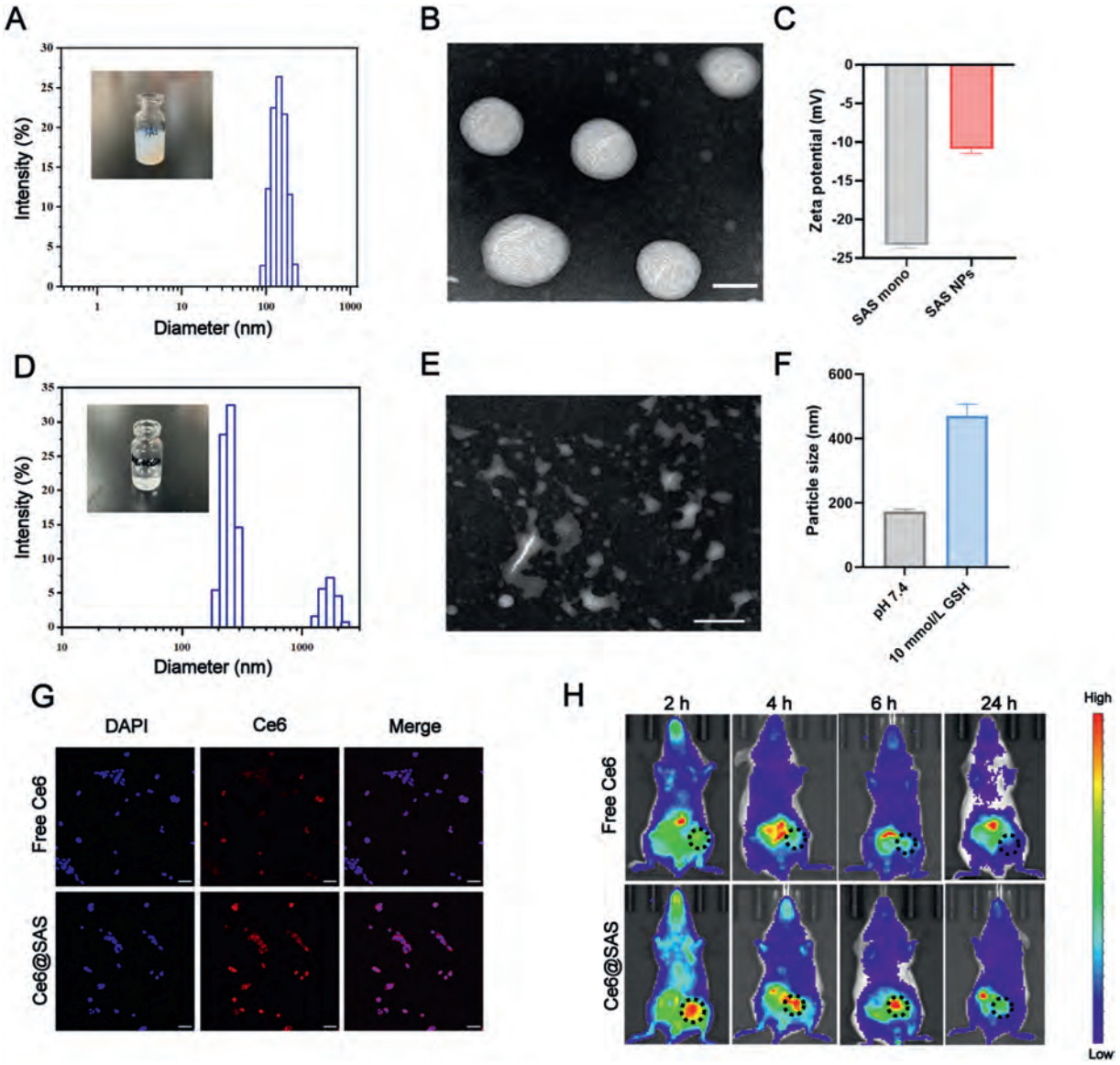

Figure 1 Preparation and characterization of SAS nanoparticles. (A) DLS particle size and photographs of SAS nanoparticles. (B) TEM images of SAS nanoparticles. Scale bar = 100 nm. (C) Zeta potential of SAS monomer and nanoparticles, $n = 3$. (D) DLS particle size and photographs of SAS nanoparticles after co-incubation with 10 mmol/L GSH. (E) TEM images of SAS nanoparticles after co-incubation with 10 mmol/L GSH. Scale bar = 500 nm. (F) Particle size change after incubation under 10 mmol/L GSH environment, $n = 3$. (G) Cell uptake determined by confocal microscopy after incubation with free Ce6, Ce6@SAS. Scale bar = 100 μm. (H) *In vivo* fluorescence images of 4T1 tumor-bearing mice after administration of free Ce6 and Ce6@SAS. Data are presented as mean ± SD.

32.6%, indicating that tumor derived exosomes had significant inhibitory effect on T cell proliferation. After using SAS to treat tumor cells, the effect of isolated tumor exosomes on T cell proliferation was significantly reduced, and the positive rate reached 94.5%, which was almost consistent with the positive control group, indicating that SAS nanoparticle administration can significantly reduce the effect of exosomes on T cell proliferation. Meanwhile, the effect of tumor exosomes on T cell killing function was characterized by expression of granzyme B. $CD8^+$ T cells exposed to SAS pre-treated tumor exosomes had much higher expression of granzyme B (26.5%) compared with $CD8^+$ T cells exposed to PBS pre-treated tumor exosomes (15.3%), which suggested that SAS treatment could significantly reduce the effect of tumor exosomes on T cell killing function after inhibiting secretion of tumor exosomes (Fig. 2H and I). Similar results also appeared in the results of the effect of tumor exosomes on the killing function of $CD4^+$ T cells (Supporting Information Fig. S6). In addition to examining the effect of exosomes on T cells after different treatments, we also investigated the effect of different exosomes of the same concentration on T cell activation. As shown in Supporting Information Fig. S7, there was no significant difference in the activation level of T cells after the treatment of the same concentration of PBS pre-treated tumor exosomes and SAS pre-treated tumor exosomes to T cells, indicating that SAS played its role mainly by inhibiting the number of exosomes, and had no significant effect on the composition of exosomes.

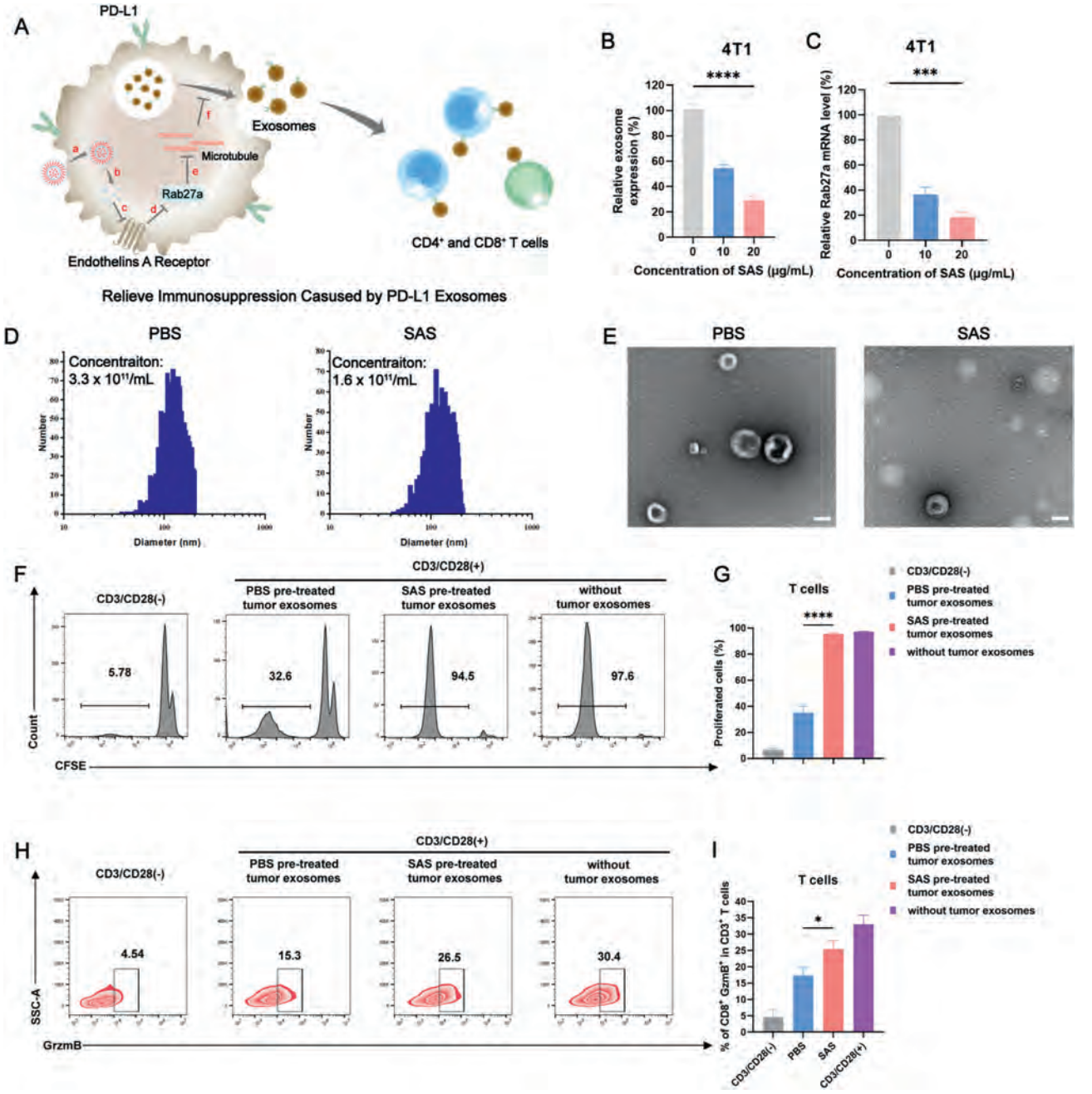

Figure 2 SAS nanoparticles inhibited exosomes secretion in 4T1 cells. (A) Schematic illustration of SAS inhibited PD-L1 exosomes secretion and relieved immunosuppression. (B) Exosomes secretion level detected by BCA assay kit, $n = 3$. (C) Relative *Rab27a* mRNA level in 4T1 cells detected by PCR method, $n = 3$. (D) Size distribution of exosomes secreted by 4T1 cells. (E) Representative TEM images of harvest exosomes from 4T1 supernatant after different treatments. Scale Bar = 100 nm. (F) Cytometry assay and (G) data analysis of CFSE-labelled $CD3^+$ T cells with different treatment in 4T1 cells, $n = 3$. (H) Cytometry assay and (I) data analysis of $GzmB^+$ in $CD3^+$ $CD8^+$T cells with different treatment, $n = 3$. Data are presented as mean ± SD; $^*P < 0.05$, $^{***}P < 0.001$, $^{****}P < 0.0001$.

3.3. Preparation and characterization of Gem@SAS nanoparticles

After successfully preparing SAS nanoparticles and verifying the function of exosomes inhibition, we further load gemcitabine (Gem) into SAS to form Gem@SAS nanoparticles, with a drug loading ability of 9.15% (Supporting Information Table S2). The Gem@SAS had a narrow size distribution and micelle-like structures, with a hydrodynamic particle size of nearly 170.9 nm and PDI value of nearly 0.274, and the zeta potential was about −8.51 mV (Fig. 3A and B). Compared with SAS nanoparticles, Gem@SAS nanoparticles had a larger particle size, which was caused by the assembly of two molecules. To further verify the assembly mechanism between Gem and SAS, sodium dodecyl sulfate (SDS) and urea were introduced to explore the involvement of hydrophobic interactions and hydrogen bonding in the self-

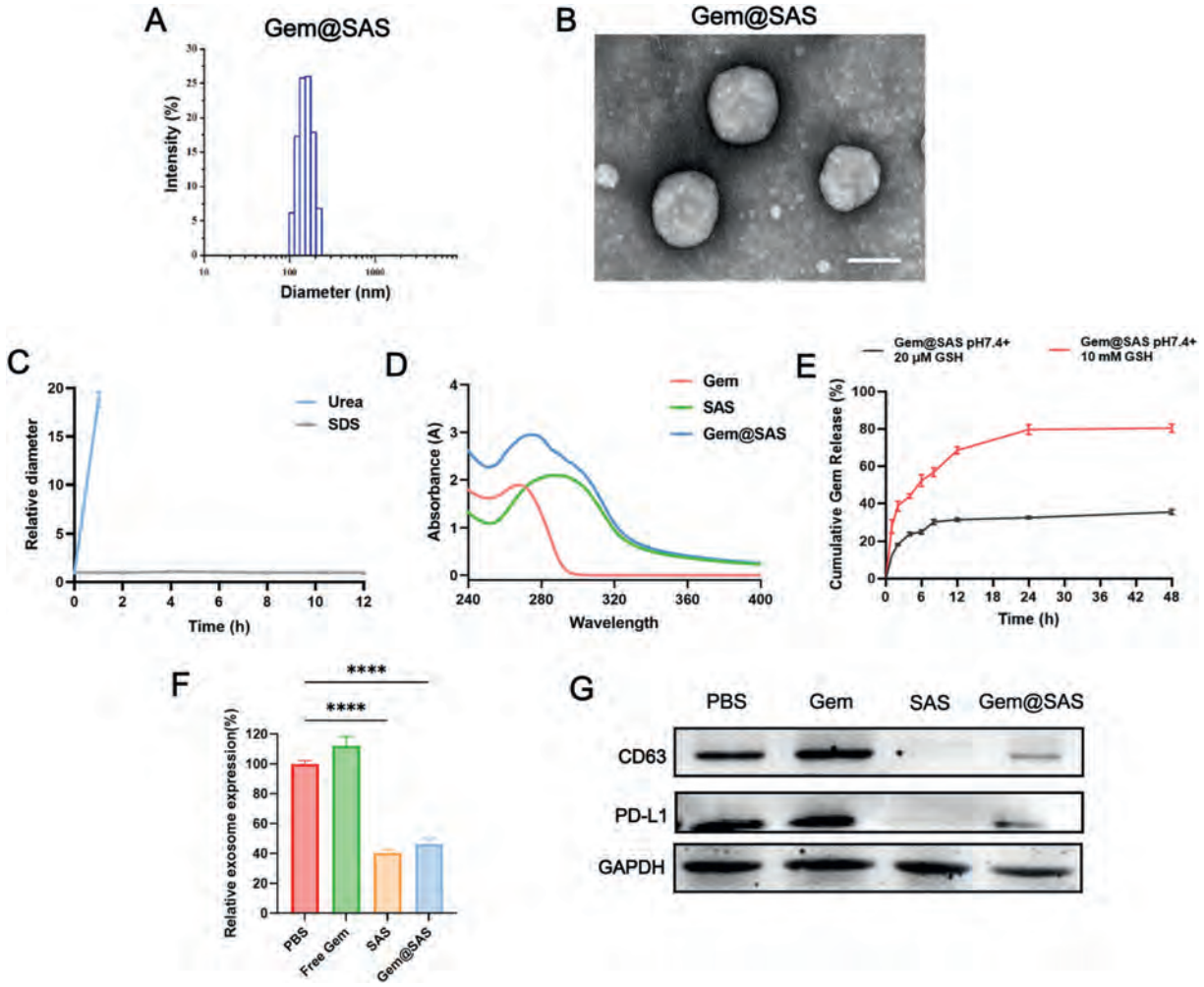

Figure 3 Preparation and characterization of Gem@SAS nanoparticles. (A) DLS particle size and photographs of Gem@SAS nanoparticles. (B) TEM images of Gem@SAS nanoparticles. Scale bar = 100 nm. (C) Changes in the particle size of Gem@SAS nanoparticles treated with urea or SDS. (D) The UV−Vis absorption spectra of Gem, SAS and Gem@SAS. (E) *In vitro* release behavior of Gem@SAS at pH 7.4 + 20 μmol/L GSH or pH 7.4 + 10 mmol/L GSH, $n = 3$. (F) Exosomes secretion level detected by BCA assay kit, $n = 3$. (G) Western blotting analysis of GAPDH, CD63 and PD-L1 expression after different treatment in 4T1 cells derived exosomes. Data are presented as mean ± SD; ****$P < 0.0001$.

assembly process. As shown in Fig. 3C, the particle size increased significantly in urea solution but remained unchanged in SDS solution, indicating that hydrogen bonding might exist between Gem and SAS. Meanwhile, in Fig. 3D of UV spectrum, the absorption peaks of Gem and SAS existed simultaneously, which also indicated the successful assembly between Gem and SAS. Moreover, due to the presence of disulfide bonds in the drug, the glutathione (GSH) responsive release ability of Gem was investigated. As demonstrated in Fig. 3E, minimal drug release occurred in the presence of 20 μmol/L GSH, while the release rate of Gem significantly increased in the presence of 10 mmol/L GSH, rising from approximately 27%−80% within 48 h.

We also investigated the exosomes inhibitory ability of the drugs after their incorporation into Gem@SAS nanoparticles. The concentration of exosomes in tumor cell supernatant after different treatments was determined by BCA method. As shown in Fig. 3F, exosomes concentrations increased slightly after Gem treatment. This may be attributed to endoplasmic reticulum stress induced by Gem, which triggered the unfolded protein response, enhanced the formation of multivesicular bodies, and ultimately led to an up-regulation in exosomes secretion. However, we found that tumor exosomes were significantly decreased after Gem@SAS treatment, indicating that the presence of SAS effectively reversed the increased secretion of tumor exosomes caused by Gem treatment. In addition, Western blot was applied to analyze the levels of tumor exosomes after different treatments, and the detected proteins were GAPDH (as an internal reference protein) CD63 (as an exosomes marker protein) and PD-L1 protein. As shown in Fig. 3G, after SAS and Gem@SAS administration, the expression of CD63 and PD-L1 were significantly decreased, indicating that SAS had excellent ability to inhibit exosomes secretion.

3.4. Gemcitabine loaded SAS nanoparticles for enhanced immunogenic cell death and DC maturation

After successfully loading gemcitabine into SAS nanoparticles, we further investigated the mechanism of activation of immune efficacy (Fig. 4A). We first examined the cytotoxicity of free gemcitabine, SAS nanoparticles and Gem@SAS nanoparticles on 4T1 cells by methylthiazolyltetrazolium (MTT) assay. As shown in Fig. 4B and Supporting Information Fig. S8, the IC_{50} values were approximately 25.64 μg/mL for SAS and 0.62 μg/mL for

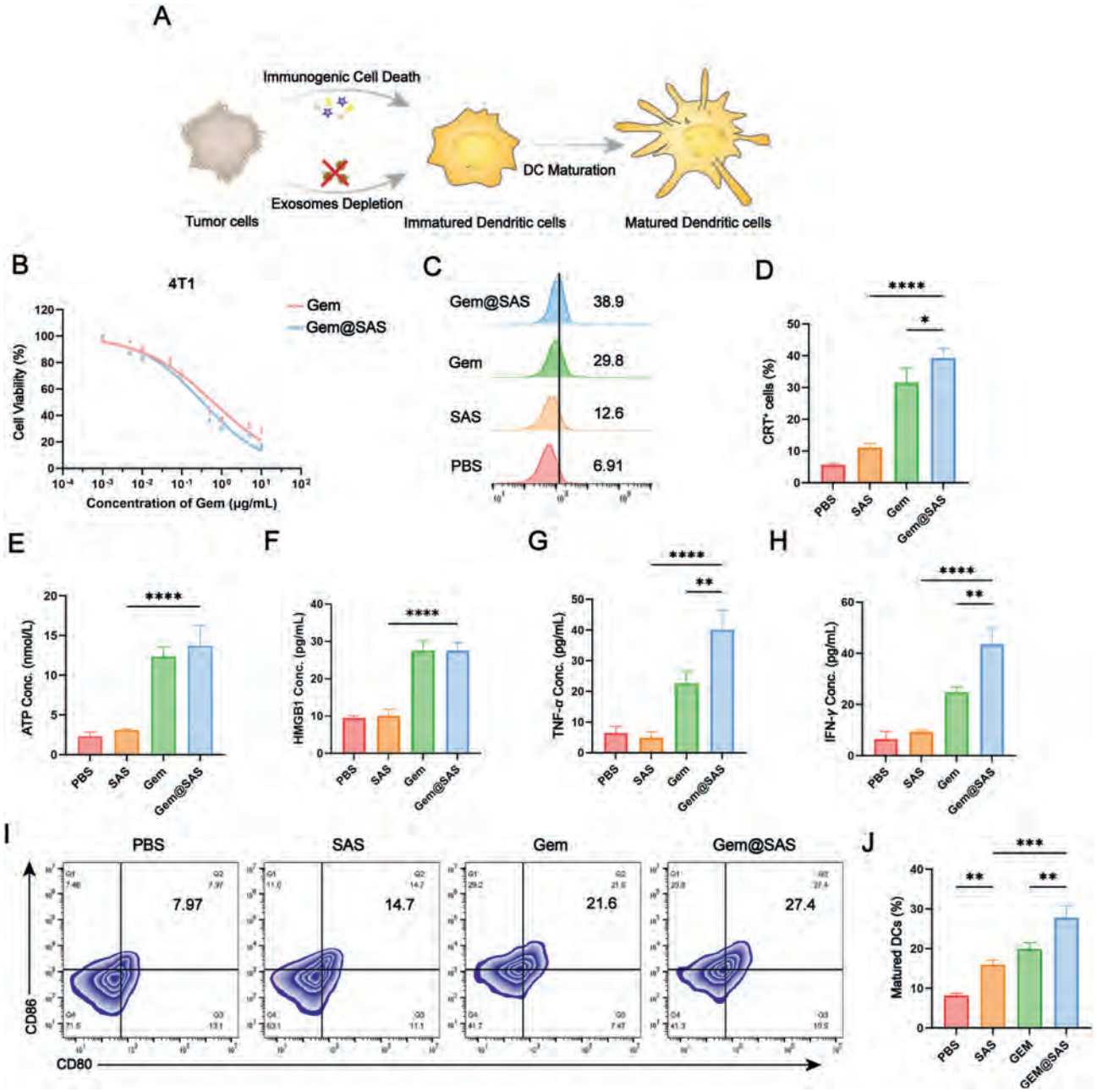

Figure 4 Gem@SAS triggered immunogenic cell death in 4T1 cells. (A) Schematic illustration of ICD effect and exosomes depletion triggered DC maturation. (B) Cell viability of 4T1 cells after incubation with Gem or Gem@SAS, $n = 3$. (C) Cytometry assay and (D) data analysis of CRT^+ cells with different treatments in 4T1 cells, $n = 3$. (E) ATP continent in cellular medium with different treatments in 4T1 cells, $n = 3$. (F) HMGB1 continent in cellular medium with different treatments in 4T1 cells, $n = 3$. (G) IFN-γ and (H) TNF-α in cell culture supernatant detected by ELISA kits, $n = 3$. (I) Cytometry assay and (J) data analysis of DC maturation after incubation with the 4T1 cells post-treatment, $n = 3$. Data are presented as mean ± SD; $^*P < 0.05$, $^{**}P < 0.01$, $^{***}P < 0.001$, $^{****}P < 0.0001$.

free gemcitabine, indicating that the cytotoxicity of SAS NPs was much lower than that of free gemcitabine. Furthermore, the IC_{50} value of Gem@SAS NPs was approximately 0.33 μg/mL, and the combination index was 0.66, which suggested gemcitabine had a slight synergistic effect with SAS. Meanwhile, cell apoptosis determined by Annexin V-FITC/PI double staining showed similar results with MTT assay, in which Gem@SAS induced the strongest cell apoptosis (30.24%) (Supporting Information Fig. S9).

Notably, chemotherapy drug gemcitabine could induce ICD, which elicits an immune response in the body. To validate this, classical ICD markers such as CRT, ATP and HMGB1 were detected after different treatments (Fig. 4C–F). As shown in the results, compared with the control group, gemcitabine boosted CRT explosion on the cell surface, and SAS NPs could also trigger slightly higher CRT positive cells (Fig. 4C and D). Similar variations in ATP and HMGB1 secretion levels among the control group and gemcitabine group corresponded to CRT. Furthermore, DC maturation induced by ICD was determined by co-incubating DC cells with 4T1 cells after different treatments. TNF-α and IFN-γ played important roles in DC maturation, and the level of

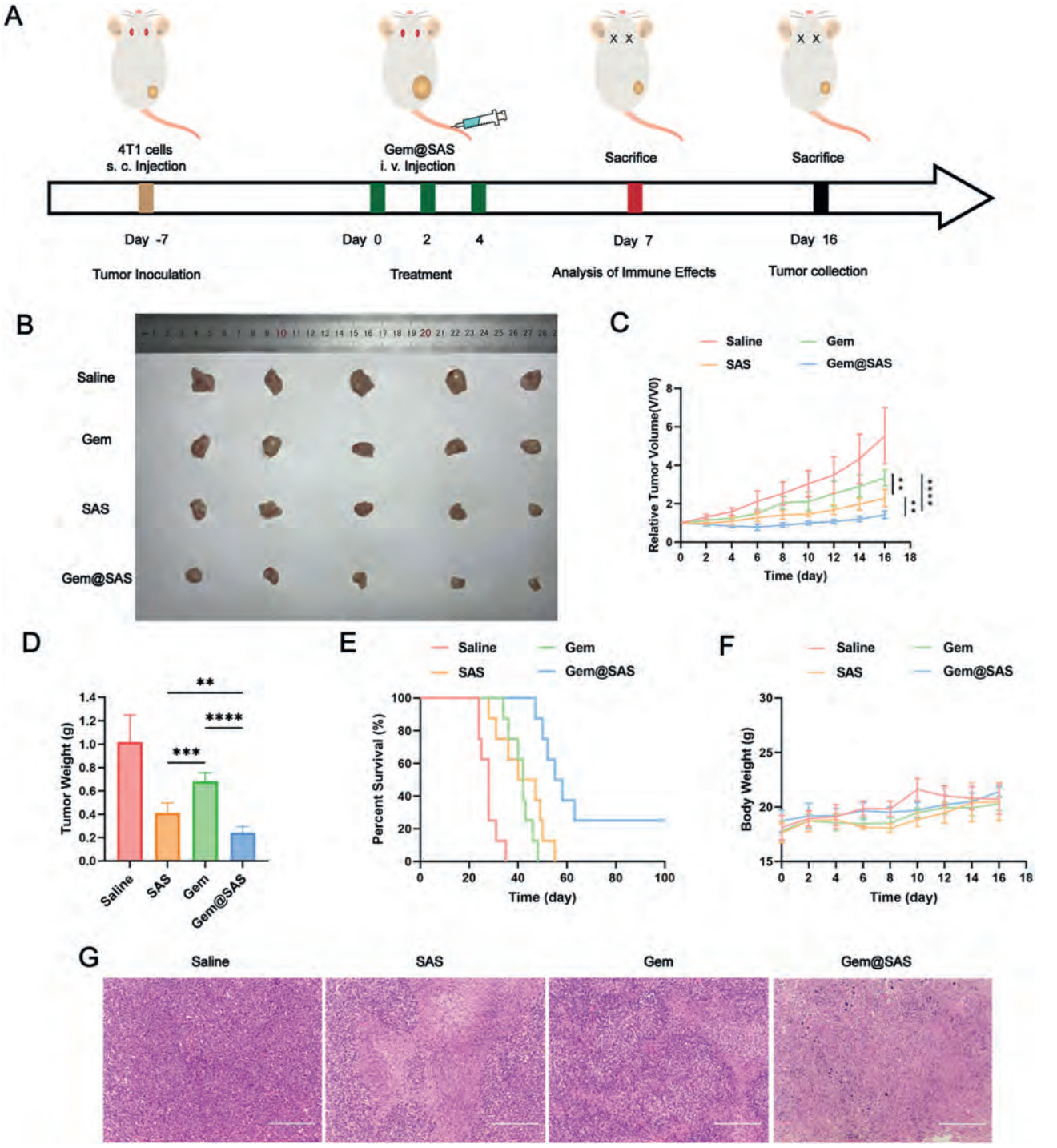

Figure 5 Antitumor efficacy of Gem@SAS in 4T1 tumor-bearing mice. (A) Schematic illustration of treatment schedule. (B) Representative images of *ex vivo* tumors on Day 16. (C) Tumor growth curve of 4T1 model after treatment with saline, Gem, SAS or Gem@SAS, $n = 5$. (D) Tumor weight on Day 16 after treatment with saline, Gem, SAS or Gem@SAS, $n = 5$. (E) The survival percentage of the tumor-bearing BALB/c mice, $n = 8$. (F) Body weight monitoring of mice during treatment, $n = 5$. (G) H&E staining of tumor sections after treatment with saline, Gem, SAS or Gem@SAS. Scale bar = 200 μm. Data are presented as mean ± SD; $^{**}P < 0.01$, $^{***}P < 0.001$, $^{****}P < 0.0001$.

TNF-α and IFN-γ in cell culture supernatant were detected by the ELISA kits. As shown in Fig. 4G and H, the cytokine content in the cell supernatant was significantly up-regulated after Gem@SAS treatment. In Fig. 4I and J, the DC maturation ratio was 27.4% in the Gem@SAS group, which was higher than that of SAS (14.7%) and Gem (21.6%) treatment group. It has been reported that tumor cells derived exosomes had the ability to inhibit DC maturation, thus exosomes inhibition strategy could significantly potentiate the efficacy of chemotherapy induced ICD.

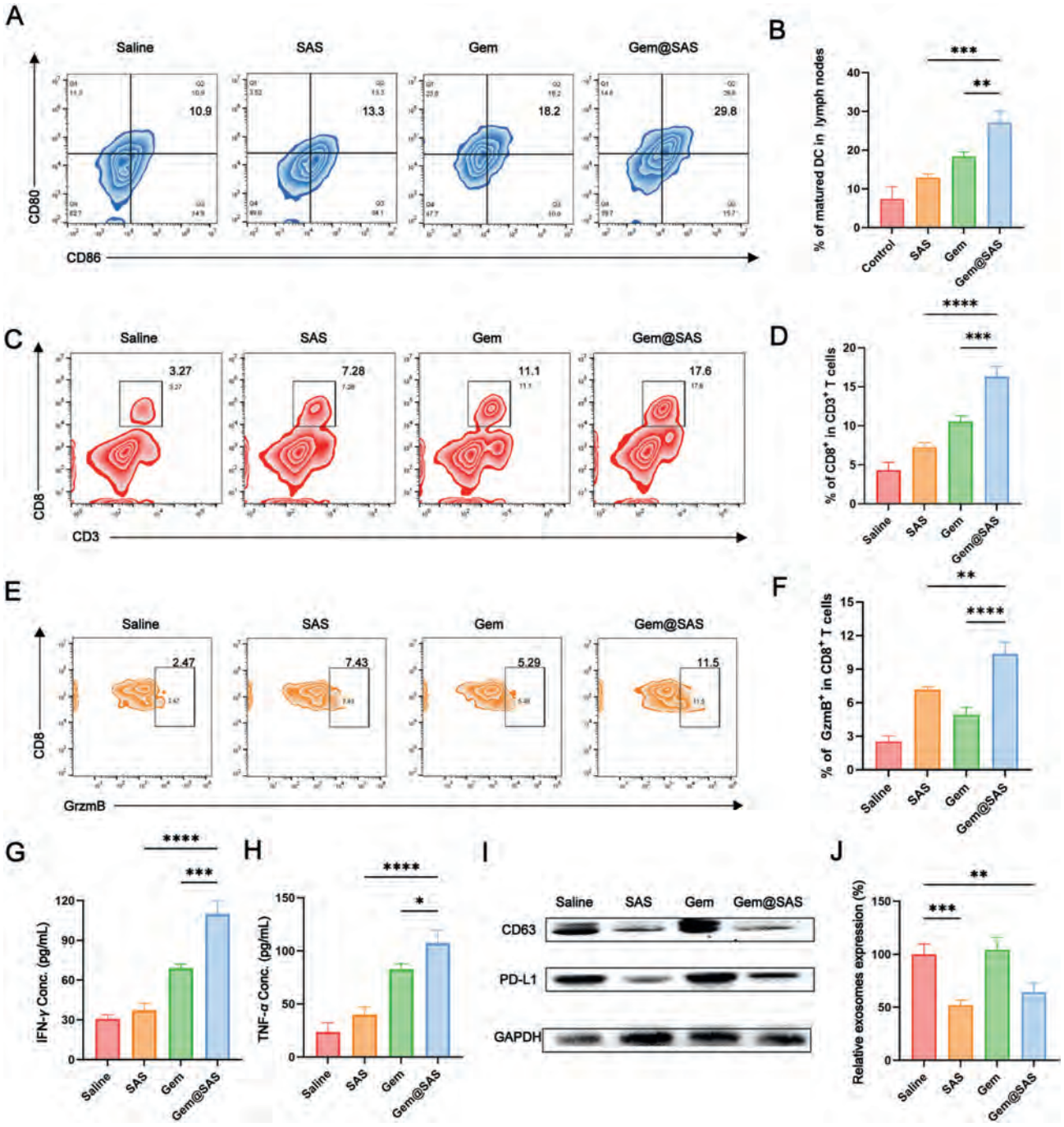

Figure 6 Immune activation of Gem@SAS in 4T1 tumor-bearing mice. (A) Cytometry assay and (B) data analysis of *in vivo* DC maturation ($CD11c^+MHC\text{-}II^+CD80^+CD86^+$) with different treatment from lymph node in 4T1 model, $n = 3$. (C) Cytometry assay and (D) data analysis of *in vivo* $CD8^+$ T cells infiltration ($CD45^+CD3^+CD8^+$) with different treatment from tumors in 4T1 model, $n = 3$. (E) Cytometry assay and (F) data analysis of $GrzmB^+$ in $CD8^+$ T cells ($CD45^+CD3^+CD4^+GrzmB^+$) with different treatment from lymph nodes in 4T1 model, $n = 3$. (G) IFN-γ and (H) TNF-α in serum on Day 7 detected by ELISA kits, $n = 3$. (I) Exosomes secretion level in the blood detected by BCA assay kit, $n = 3$. (J) Western blotting analysis of GAPDH, CD63 and PD-L1 expression after different treatment in the blood of 4T1 tumor bearing mice. Data are presented as mean ± SD; $^*P < 0.05$, $^{**}P < 0.01$, $^{***}P < 0.001$, $^{****}P < 0.0001$.

3.5. In vivo antitumor therapy and immune activation

To further investigate the therapeutic efficacy of Gem@SAS, 4T1 tumor-bearing model was constructed. The treatment schedule was shown in Fig. 5A, where Gem@SAS was administrated in three doses on Days 0, 2 and 4 by intravenous (i.v.) injection.

As shown in Fig. 5B and C and Supporting Information Fig. S10, tumor grew rapidly and reached a volume 6-fold greater than the original volume when untreated. Compared with the saline group, SAS and Gem only produced a weak therapeutic effect. Among them, the tumor volume of Gem treatment group reached 500 mm^3 on Day 16, which was about 3.3-fold of the

initial tumor volume, and in SAS treatment group, the tumor volume reached 350 mm^3 on Day 16, which was 2.3-fold of the initial. Meanwhile, Gem@SAS had the strongest anti-tumor efficacy, with tumor volume only about 20% of the control group on Day 16. As calculated by tumor weight on Day 16 (Fig. 5D), the tumor inhibition ratio of Gem@SAS was 75%. What's more, compared with the median survival of 28 days in the saline group, the median survival of the Gem and SAS treatment groups were extended to 42 and 46.5 days, respectively. Meanwhile, the median survival of the Gem@SAS group was extended to 56.5 days (Fig. 5E), and tumors of two mice completely disappeared, indicating the superior anti-tumor effects of Gem@SAS. Therapeutic biosafety could be reflected in the body weight during treatment and the healthy organ status (Fig. 5F and Supporting Information Fig. S11). Likewise, apparent apoptosis and necrosis morphology were observed in H&E staining images of tumor sections after treatment with Gem@SAS (Fig. 5G).

In vivo immune activation was analyzed on Day 7 after the initial injection. DC maturation in lymph nodes was evaluated by analyzing the $CD80^+CD86^+$ cell ratios. As is exhibited in Fig. 6A and B, Gem@SAS had the highest ability to induce DC maturation at 29.8%, more than 2.7-fold higher than the saline group. In addition, tumors were collected and the $CD3^+CD8^+$ T cells were analyzed. Gem@SAS induced the highest increase in tumor-infiltrating cytotoxic T lymphocytes, reaching a rate of 17.6%, more than 5.3-fold that of the saline group (Fig. 6C and D), due to PD-L1 exosomes inhibition and enhanced immunogenic cell death. What's more, the activation of T cells was further explored by analyzing the cellular activation marker Granzyme B (Fig. 6E and F and Supporting Information Fig. S12). Notably, the $GrzmB^+$ ratio of $CD8^+$ T cells also reached 16.1% and that of $CD4^+$ T cells 15.8% in the SAS treatment group, which further confirmed that the PD-L1 exosomes inhibition strategy could effectively alleviate immunosuppression. And Gem@SAS showed the highest percentage of Granzyme B positive in both $CD8^+$ T cells (21.2%) and $CD4^+$ T cells (20.5%). In addition, the highest level of IFN-γ and TNF-α in mice serum were observed after Gem@SAS treatment (Fig. 6G and H), indicating that Gem@SAS had the capacity to elicit an efficient proinflammatory factor response. Furthermore, treatment with Gem@SAS was the most effective in increasing the frequencies of tumor-infiltrating $CD3^+$ T cells, but had no significant effect on $CD4^+$ T cells (Supporting Information Fig. S13).

The level of exosomes and PD-L1 protein expression in mouse serum were investigated by Western blotting (Fig. 6I), the results demonstrated that subsequent to SAS treatment, the CD63 protein level was markedly diminished, signifying that SAS was capable of significantly impeding the release of exosomes. The reduction in the PD-L1 protein level indicated that the level of PD-L1 exosomes within the blood circulation was substantially decreased, thereby alleviating the immunosuppression issue induced by exosomes. Moreover, consistent with the Western blotting results, the levels of exosomes in the blood of mice were also significantly down regulated after SAS treatment, which was about 50% lower than that in the control group (Fig. 6J).

To further confirm the anti-metastasis effect of Gem@SAS, a lung metastasis model 4T1 model was established by injecting 4T1 cells into BALB/c mice intravenously. The treatment was the same as mentioned above and lung tissues were harvested on Day 16. It should be noted that the strong exosomes secretion inhibition and immune activation by Gem@SAS effectively prevented the metastasis of 4T1 tumor cells, with minimal metastatic foci and the smallest metastatic area (Supporting Information Fig. S14).

4. Conclusions

In summary, a novel carrier-free nanomedicine, composed of sulfafurazole homodimers (SAS), was successfully developed for delivery of gemcitabine, offering a synergistic approach to anti-tumor chemotherapy and immunotherapy. Gem@SAS NPs were easy to prepare and had a high drug loading capacity. The disulfide bonds within nanoparticles facilitated a GSH-responsive release of the drug, thus avoiding systemic toxicity of the formulation. Moreover, on the one hand, Gem@SAS used low-dose gemcitabine as the ICD promoter, which induced tumor immunogenic cell death and recruited T cells to kill tumors; on the other hand, it inhibited exosomes secretion through the down-regulation of the expression of Rab27a, a key factor for exosomes secretion regulation in tumor cells. Notably, the inhibition of PD-L1 exosomes secretion improved the vitality and cytotoxicity of T cells, so as to increase the efficacy of anti-tumor immunotherapy.

In addition to gemcitabine, other therapeutic agents capable of inducing ICD *in vivo*, such as paclitaxel, doxorubicin and chlorin e6, also hold promising application prospects when combined with SAS. Meanwhile, apart from breast cancer, melanoma, pancreatic cancer, and other tumors also possess the ability to secrete a large number of exosomes, which promote tumor growth. Therefore, SAS nanoparticles also have the potential for application in other tumor models.

However, during the application of SAS, we have also encountered some issues. The highly hydrophobic structure of SAS renders it difficult to remain stable *in vitro* for an extended period. Modifying hydrophilic molecules like PEG on its surface might resolve this problem. Meanwhile, SAS will unavoidably act on other cells within the body, and the subsequent inhibition of exosomes release could potentially pose other functional risks to the body. Hence, further research is required to conduct a comprehensive evaluation of its efficacy.

Acknowledgments

This work was financially supported by the National Natural Science Foundation of China (82473866 and 32471394), Key Research and Development Program Social Development Project of Jiangsu Province (BE2023845, China) and Natural Science Foundation of Jiangsu Province (BK20210424, China).

Author contributions

Zheng Wang, Zhanwei Zhou and Minjie Sun designed the experiments. Zheng Wang, Ronghui Yin, Lin Zhang and Shiyu Li performed the experiments and collected the data. Zheng Wang contributed to writing the manuscript and analyzing the results. Minjie Sun and Zhanwei Zhou revised the final manuscript. All of the authors have read and approved the final manuscript.

Conflicts of interest

The authors have no conflicts of interest to declare.

Appendix A. Supporting information

Supporting information to this article can be found online at https://doi.org/10.1016/j.apsb.2025.03.007.

References

1. Doroshow DB, Bhalla S, Beasley MB, Sholl LM, Kerr KM, Gnjatic S, et al. PD-L1 as a biomarker of response to immune-checkpoint inhibitors. *Nat Rev Clin Oncol* 2021;**18**:345−62.
2. Yamaguchi H, Hsu JM, Yang WH, Hung MC. Mechanisms regulating PD-L1 expression in cancers and associated opportunities for novel small-molecule therapeutics. *Nat Rev Clin Oncol* 2022;**19**:287−305.
3. Hu C, Song YJ, Zhang YW, He SQ, Liu XY, Yang XT, et al. Sequential delivery of PD-1/PD-L1 blockade peptide and Ido inhibitor for immunosuppressive microenvironment remodeling *via* an MMP-2 responsive dual-targeting liposome. *Acta Phar Sin B* 2023;**13**: 2176−87.
4. Morad G, Helmink BA, Sharma P, Wargo JA. Hallmarks of response, resistance, and toxicity to immune checkpoint blockade. *Cell* 2021; **184**:5309−37.
5. Chen G, Huang AC, Zhang W, Zhang G, Wu M, Xu W, et al. Exosomal PD-L1 contributes to immunosuppression and is associated with anti-PD-1 response. *Nature* 2018;**560**:382−6.
6. Cordonnier M, Nardin C, Chanteloup G, Derangere V, Algros MP, Arnould L, et al. Tracking the evolution of circulating exosomal-PD-L1 to monitor melanoma patients. *J Extracell Vesicles* 2020;**9**: 1710899.
7. Poggio M, Hu TY, Pai CC, Chu B, Belair CD, Chang A, et al. Suppression of exosomal PD-L1 induces systemic anti-tumor immunity and memory. *Cell* 2019;**177**:414−27.
8. Kalluri R, LeBleu VS. The biology, function, and biomedical applications of exosomes. *Science* 2020;**367**:eaau6977.
9. Li Q, Guo L, Wang J, Tao SJ, Jin PS. Exosomes derived from Nr-CWS pretreated MSCs facilitate diabet-ic wound healing by promoting angiogenesis *via* the circIARS1/miR-4782-5p/VEGFA axis. *Chin J Nat Med* 2023;**21**:172−84.
10. Pavlakis E, Neumann M, Stiewe T. Extracellular vesicles: messengers of p53 in tumor−stroma communication and cancer metastasis. *Int J Mol Sci* 2020;**21**:9648.
11. Zhou JR, Li XD, Wu XL, Zhang T, Zhu QY, Wang XJ, et al. Exosomes released from tumor-associated macrophages transfer miRNAs that induce a Treg/Th17 cell imbalance in epithelial ovarian cancer. *Cancer Immunol Res* 2018;**6**:1578−92.
12. Daassi D, Mahoney KM, Freeman GJ. The importance of exosomal PDL1 in tumour immune evasion. *Nat Rev Immunol* 2020;**20**:209−15.
13. Hood JL. The association of exosomes with lymph nodes. *Semin Cell Dev Biol* 2017;**67**:29−38.
14. Hood JL, Roman SS, Wickline SA. Exosomes released by melanoma cells prepare sentinel lymph nodes for tumor metastasis. *Cancer Res* 2011;**71**:3792−801.
15. Srinivasan S, Vannberg FO, Dixon JB. Lymphatic transport of exosomes as a rapid route of information dissemination to the lymph node. *Sci Rep* 2016;**6**:24436.
16. Chen JM, Yang J, Wang WH, Guo DF, Zhang CY, Wang SB, et al. Tumor extracellular vesicles mediate anti-PD-L1 therapy resistance by decoying anti-PD-L1. *Cell Mol Immunol* 2022;**19**:1290−301.
17. Wang YZ, Zhou Y, Yang LY, Lei L, He B, Cao J, et al. Challenges coexist with opportunities: spatial heterogeneity expression of PD-L1 in cancer therapy. *Adv Sci* 2024;**11**:e2303175.
18. Alam MR, Rahman MM, Li ZG. The link between intracellular calcium signaling and exosomal PD-L1 in cancer progression and immunotherapy. *Genes Dis* 2024;**11**:321−34.
19. Xie FT, Xu MX, Lu J, Mao LX, Wang SJ. The role of exosomal PD-L1 in tumor progression and immunotherapy. *Mol Cancer* 2019;**18**:146.
20. Wu MW, Wang GS, Hu WL, Yao YH, Yu XF. Emerging roles and therapeutic value of exosomes in cancer metastasis. *Mol Cancer* 2019; **18**:53.
21. Park JH. Regulation of *in vivo* fate of exosomes for therapeutic applications: new frontier in nanomedicines. *J Control Release* 2022; **348**:483−8.
22. Li Y, Chen ZK, Duan X, Zhang HJ, Xiao BL, Wang KM, et al. Targeted inhibition of tumor-derived exosomes as a novel therapeutic option for cancer. *Exp Mol Med* 2022;**54**:1379−89.
23. Im EJ, Lee CH, Moon PG, Rangaswamy GG, Lee B, Lee JM, et al. Sulfisoxazole inhibits the secretion of small extracellular vesicles by targeting the endothelin receptor A. *Nat Commun* 2019;**10**:1387.
24. Shin JM, Lee CH, Son S, Kim CH, Lee JA, Ko H, et al. Sulfisoxazole elicits robust antitumour immune response along with immune checkpoint therapy by inhibiting exosomal PD-L1. *Adv Sci* 2022;**9**:e2103245.
25. Huang JW, Ma XY, Liao ZX, Liu ZL, Wang KY, Feng ZY, et al. Network pharmacology and experimental validation of Maxing Shigan decoction in the treatment of influenza virus-induced ferroptosis. *Chin J Nat Med* 2023;**21**:775−88.
26. Zhang CP, Chen XY, Wei TC, Song J, Tang XJ, Bi J, et al. Xuebijing alleviates LPS-induced acute lung injury by downregulat-ing pro-inflammatory cytokine production and inhibiting gasder-min-E-mediated pyroptosis of alveolar epithelial cells. *Chin J Nat Med* 2023;**21**:576−88.
27. Duan XP, Chan C, Lin WB. Nanoparticle-mediated immunogenic cell death enables and potentiates cancer immunotherapy. *Angew Chem Int Ed Engl* 2019;**58**:670−80.
28. Kroemer G, Galassi C, Zitvogel L, Galluzzi L. Immunogenic cell stress and death. *Nat Immunol* 2022;**23**:487−500.
29. Chen DS, Mellman I. Oncology meets immunology: the cancer-immunity cycle. *Immunity* 2013;**39**:1−10.
30. Li HN, Gong QY, Luo K. Biomarker-driven molecular imaging probes in radiotherapy. *Theranostics* 2024;**14**:4127−46.
31. Liu JY, Bai YN, Li YG, Li XL, Luo K. Reprogramming the immunosuppressive tumor microenvironment through nanomedicine: an immunometabolism perspective. *Ebiomedicine* 2024;**107**:105301.
32. Fu SW, Li GT, Zang WL, Zhou XY, Shi KX, Zhai YL. Pure drug nano-assemblies: a facile carrier-free nanoplatform for efficient cancer therapy. *Acta Pharm Sin B* 2022;**12**:92−106.
33. Liu LH, Zhang XZ. Carrier-free nanomedicines for cancer treatment. *Prog Mater Sci* 2022;**125**:100919.
34. Mei H, Cai SS, Huang DN, Gao HL, Cao J, He B. Carrier-free nanodrugs with efficient drug delivery and release for cancer therapy: from intrinsic physicochemical properties to external modification. *Bioact Mater* 2022;**8**:220−40.
35. Li HN, Zang WL, Mi Z, Li JY, Wang LJ, Xie D, et al. Tailoring carrier-free nanocombo of small-molecule prodrug for combinational cancer therapy. *J Control Release* 2022;**352**:256−75.
36. Huang L, Zhao SJ, Fang F, Xu T, Lan MH, Zhang JF. Advances and perspectives in carrier-free nanodrugs for cancer chemo-monotherapy and combination therapy. *Biomaterials* 2021;**268**:120557.